Journal of Materials Chemistry

Cite this: J. Mater. Chem., 2012, 22, 1868

www.rsc.org/materials

PAPER

Multilevel conductance switching for a monolayer of redox-active metal complexes through various metallic contacts†

Sohyeon Seo,[a] Junghyun Lee,[a] Sung-Yool Choi[b] and Hyoyoung Lee*[a]

Received 22nd September 2011, Accepted 3rd November 2011
DOI: 10.1039/c1jm14715c

Redox-active metal complexes (*e.g.*, Fe^{II}, Ru^{II}, and Co^{II} biphenylterpyridine) exhibiting multiple electroreduction behaviors show multilevel conductance switching through various metallic contacts, including Au, Pt/Ir, and reduced graphene oxide (rGO), in solid-state molecular junctions (*e.g.*, a metal–molecule–metal junction). At Pt/Ir and Au contacts in the scanning tunneling microscopy (STM)-based junctions or Au/rGO film contacts in monolayer-based devices, current–voltage (*I*/*V*) characteristics have different energy distributions depending on the level of injection into the three electron affinity levels of the redox-active metal complexes. These metal complexes can be negatively charged when the energy levels between the Fermi levels of the metal contacts and the molecular reduction states are aligned, which strongly depends upon the molecular conductance states of conjugated ligands coordinated to central metal atoms. Multiple reduction states of redox-active metal complexes measured with solution-phase electrochemistry correspond to the multiple electron affinity levels of the solid-state molecular junctions, which suggests the possibility of multilevel molecular memory components.

Introduction

To design molecular electronic devices, it is necessary to understand the relationship between the molecular electronic structure and the chemical and electrical events in the solid state.[1] Molecular effects in electronic components can be observed by measuring voltage–current (*I*/*V*) characteristics in a molecular junction of molecules vertically sandwiched between contact electrodes.[2] Furthermore, the energy relationship between molecules and contact metal electrodes in the molecular junction can provide direct information about the molecular charged states of a redox-active molecule in the solid-state.[3]

Redox-active functionalized molecules have distinct charged states that can control transport properties *via* molecule-based junctions. Depending on the molecular level accessed at the Fermi level of the metal electrode, whether it is the highest occupied molecular orbital (HOMO) or the lowest unoccupied molecular orbital (LUMO), redox-active metal complexes can display molecular conduction,[4–6] switching functions,[7–9] negative differential resistance (NDR),[10] or Kondo effects.[11] Furthermore, potential-induced changes in the molecular oxidation states contribute to changes in the conductivity of redox-active molecules such as quinine-modified oligo(phenylene vinylene),[12] bipyridinium,[13] aniline oligomer,[14] oligo(phenylene ethynylene)s,[1,15] and transition metal complexes.[16] The molecular charged states in the solid state were probed by observing molecular conductance changes in scanning tunneling microscopy (STM) images[12] and *I*/*V* characteristics such as conductance switching[1] or NDR peaks,[1,14] which occurred due to molecular electrochemical behavior.

In particular, redox-active metal complexes have been considered as potential memory elements based on their behaviors in the solid state.[7,9,17,18] Molecular conductance states of metal complexes that donate or accept electrons[7,9,18,19] were probed by energy alignments of the contact Fermi level to ionization energy levels (*e.g.*, HOMO) or electron affinity levels (*e.g.*, LUMO) of the molecules. As a result, molecular conduction of the metal complexes with a conjugated ligand occurs due to electron donation in a metal-centered HOMO[4,20] or an electron acceptor in a ligand centered LUMO.[7,9] Therefore, the conduction behaviors of the metal complexes are related to the redox states induced by discrete redox centers formed by coordination of a proper ligand to a metal center. For example, the memory effect of metal complexes was reported as two redox origins of the reduction behavior of the ligand[17] and the oxidation behavior of the center metal.[19]

[a]*National Creative Research Initiative, Center for Smart Molecular Memory, Department of Chemistry, Samsung-SKKU Graphene Center, Sungkyunkwan University, 300 Cheoncheon-Dong, Jangan-Gu, Suwon, Gyeonggi-Do, 440-746, Korea. E-mail: hyoyoung@skku.edu; Fax: +82 31 290 5934; Tel: +82 31 299 4566*
[b]*Department of Electrical Engineering, KAIST, 291 Daehakro, Yuseong-gu, 305-701, Korea*

† Electronic supplementary information (ESI) available: Fig. S1, Raman spectra and XPS spectra of GO/rGO; Fig. S2, *I*/*V* curves of $M_T^{II}(tpyphs)_2$ at the Au tip; Fig. S3, AFM image of an rGO film/$M_T^{II}(tpyphs)_2$ SAM/Au device; Fig. S4, *I*/*V* curves of Au/rGO film/$M_T^{II}(tpyphs)_2$ SAM/Au devices and histograms for threshold voltage. See DOI: 10.1039/c1jm14715c

Furthermore, metal complexes with conjugated polypyridine ligands such as terpyridine have multiple electron accepting states. Based on the electron transport behavior of a molecular memory component, electron trapping in molecules should occur in molecular reduction states. Thus, multiple-electron charges in metal complexes that can undergo localized multiple reduction steps[21] would result in multilevel conductance switching (or memory). At single molecular levels, multilevel switching can effectively increase the density of memory bits and allow operations at higher levels than binary levels.[22,23] However, extraction of distinct multilevel states from single molecule measurements must consider contact effects at the interfaces of molecules and metal electrodes in molecular junctions (*e.g.*, a metal/molecule/metal junction).[3,9] Because electron transmission through the molecular junctions is strongly influenced by the coupling of molecules and metal contacts, the electronic properties of molecules may not be confined to intrinsic molecular levels but may include electrostatic image charge effects. Therefore, true molecular electronic states in a solid-state-based molecular junction need to be explored by testing various metallic contacts in reliable monolayer molecular junctions.

Herein, we report the statistical analysis of multilevel conductance switching for redox functionalized molecules (*e.g.*, bis[4′-(4-thioacetylphenyl)-2,2′:6′,2″-terpyridinyl]$M_T^{II}(PF_6)_2$, M_T = Fe, Ru, and Co, denoted with $M_T^{II}(tpyphsAc)_2$) (Fig. 1a) using various metallic contacts (*e.g.*, Au, Pt/Ir, and Au/reduced graphene oxide (rGO)). In order to produce more localized redox states by the addition of electrons, the metal complexes were designed to have conjugated ligands with a phenyl linker. Electron injection from different metallic contacts into multilevel molecular reduction states is observed through a single-molecule junction and a monolayer-based junction. *I*/*V* curves taken from the molecular junctions of the transition metal complexes are statistically analyzed using distribution histograms of threshold conductance voltage where current reaches a maximum due to alignment of one molecular conductance level with another contact Fermi level. We estimate the electron affinity levels of each metal complex at Au and Pt/Ir contacts in STM-based single-molecular junctions. For monolayer-based junctions, rGO thin films are used to protect molecular monolayers (Fig. 1c), and Au/rGO contacts are comparable to Au contacts. The electron affinity levels obtained in the solid-state-based junctions are in good agreement with intrinsic multiple electroreduction states in solution-phase electrochemistry. The multiple-electron accepting nature of the metal complexes can lead to localized electroreductions in different molecular reduction states in the solid-state, suggesting the possibility of multilevel molecular memory components.

Experimental section

Materials

Transition metal(II) complexes $M_T^{II}(tpyphsAc)_2$ $(PF_6)_2$ were synthesized and characterized using a previously described method.[7,17] UV-Vis absorption spectra confirm the expected

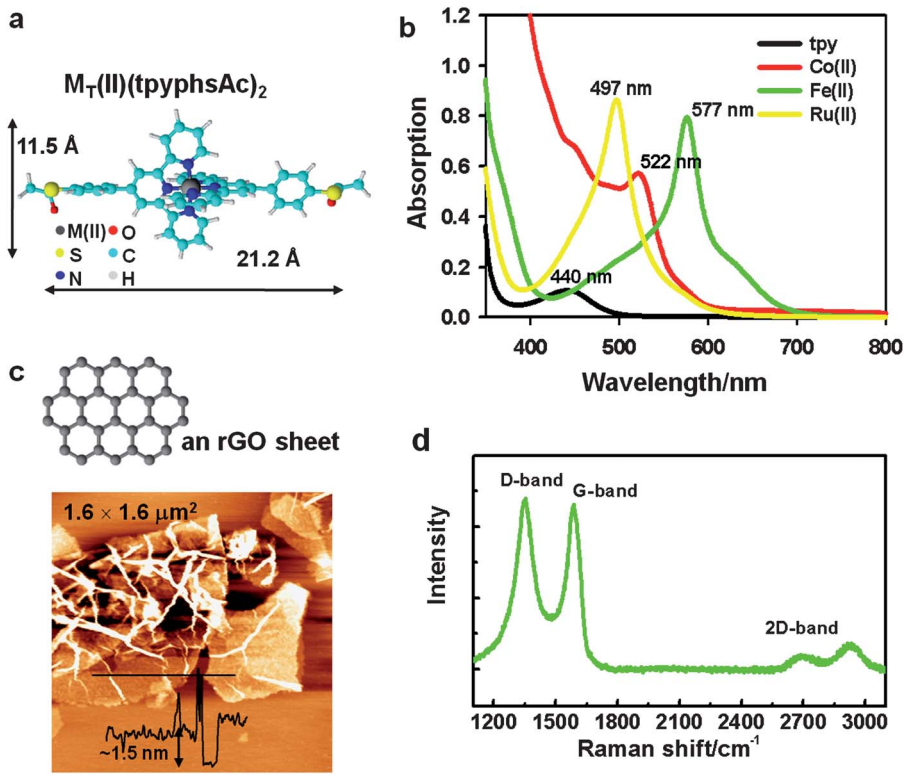

Fig. 1 (a) Structure of transition metal(II) bis-acetylthiophenylterpyridine (*i.e.*, $M_T^{II}(tpyphs)_2$) complexes. (b) UV-Vis absorption spectra of $M_T^{II}(tpyphs)_2$ complexes in DMF, which show the typical absorption of metal-to-ligand charge transfer. (c) Illustration and a topological AFM image of reduced graphene oxide (rGO) sheets. (d) Raman spectrum of an rGO film on a SiO_2 substrate, which shows the typical vibration peaks of sp^2-hybridized carbon atoms in an rGO thin film.

charge transfer behavior between the metal and the ligand in each $M_T^{II}(tpyphs)_2$ depending on the central metal atoms (Fig. 1b). Graphene oxide (GO) was synthesized by the modified Hummers method[24,25] and chemically reduced by a mixture of hydrazine and ammonia water, as described previously.[26] In the AFM image (Fig. 1c), wrinkled rGO sheets on a mica substrate were overlapped with each other in two or three of the layers. The thickness of double rGO sheets was measured at ~1.5 nm (a single rGO sheet was previously measured at 0.7–0.8 nm).[27] The Raman spectra (Fig. 1d and S1a†) and XPS spectra (Fig. S1b†) of rGO are in good agreement with previously reported data.[27]

Formation of a self-assembled monolayer (SAM)

SAMs were formed on a Au substrate, specifically a Au(111)/mica substrate from Molecular Imaging for STM and an e-beam vaporized Au/Si substrate for fabrication of devices. The Au substrates were cleaned with a hot piranha solution (1 : 3 H_2O_2 (Junsei) and H_2SO_4 (Junsei); **caution**: piranha solution is a very strong oxidant and is extremely dangerous). Then the substrates were washed with DI water and ethanol, and dried with N_2 gas. Deprotection of the thioacetate group to generate active sulfur adsorbing on Au substrates was conducted by mixing ~15 μl ammonium hydroxide (NH_4OH, Aldrich) with a 5 ml DMF solution of 3 mM $M_T^{II}(tpyphsAc)_2$ complexes. All samples of SAMs were formed by immersion of the substrates in solutions. For STM measurements of single-molecule junctions, metal complexes were isolated in a 1-dodecanethiol (C12) SAM. Thus, each mixed monolayer was formed in a mixed solution of 0.3 mM $M_T^{II}(tpyphs)_2$ complexes and 1.0 mM C12 in 24 h. The mixed SAMs were thoroughly washed with solvent and dried with N_2 gas.

STM measurements

The prepared samples were immediately transferred to an STM vacuum chamber (Omicron, VT SPM) with a background pressure $<1.2 \times 10^{-10}$ Torr. Electrochemically etched Pt/Ir tips were purchased from Molecular Imaging. Gold tips were prepared by electrochemical etching in a 30% ethanol solution of HCl. To avoid destructive tip–surface interactions, an imaging voltage range of ≤2.0 V was used in STM measurements. All STM imaging experiments for each complex were performed at 1.0–2.0 V and a 15–20 pA tunneling current in constant current mode, at which voltage the alkanethiol lattice was precisely observed. After successive STM imaging of SAMs, the *I*/*V* curves of the current response to the sample-bias voltage were measured from a molecule without tunneling current feedback (*i.e.*, scanning tunneling spectroscopy, STS). To minimize tip-artifacts during voltage sweeps, all STS data were obtained at <3.0 V, preventing destruction of the sulfur–gold bond.

UV-Vis absorption spectroscopy/electrochemistry

UV-Vis absorption spectroscopy (Hitachi, U-3501 UV/VIS/NIR spectrophotometer) and cyclic voltammetry (CHI, Electrochemical Analyzer 660A) were performed in solution. Electrochemical voltammetry was performed in an N_2 atmosphere.

Fabrication of monolayer-based devices

Au(800 nm)/Ti(5 nm)/SiO_2/Si substrates were prepared by e-beam evaporation at 0.1 Å s^{-1} for the formation of $M_T^{II}(tpyphs)_2$ SAMs. To protect the SAMs on the Au substrate, an rGO film was spin-coated onto the $M_T^{II}(tpyphs)_2$ SAMs using a 0.5 mg ml^{-1} DMF solution. The Au (60 nm) top electrode was deposited at 0.1 Å s^{-1}. The rGO film acts as a conductive blocking layer that prevents penetration of Au nanoparticles which could cause a short circuit[28] through the SAMs during evaporation of the Au top electrode. For controlled experiments with rGO film devices, an rGO film was spin-coated onto the Au substrate, and then the Au top electrode was deposited at a slow rate onto the rGO film. The electrical characteristics of the monolayer molecular devices were measured by a Keithley 4200-SCS semiconductor characterization system in a vacuum (~1.0×10^{-4} Torr).

Results and discussion

Multilevel conductance switching at Pt/Ir and Au contacts

Unlike solution-phase electrochemistry of $M_T^{II}(tpyphs)_2$, solid-phase electrochemistry[17] using SAMs cannot allow for ligand-centered electrochemical reactions in the potential window of Au substrates in solution. For solid-state measurements of molecular reduction states for $M_T^{II}(tpyphs)_2$, the electron affinity levels involved in the ligand-centered LUMOs of $M_T^{II}(tpyphs)_2$ in the solid state were obtained using solid-state molecular junctions through SAMs on Au substrates in a vacuum. Metal complexes in mixed SAMs with C12 can be isolated for single-molecule measurements. The metal complexes in the mixed SAMs were observed as protrusions in the STM images (Fig. 2a). After successive STM imaging of SAMs, STS was performed as shown in Fig. 2b. Current responses to voltage sweeps were measured from isolated metal complexes. The reliability and reproducibility of the STS measurements were confirmed using a C12 SAM on Au(111).[17] Using a Simmons metal–insulator–metal electron tunneling model,[29,30] *I*/*V* curves of C12 molecules in the bias range of $-1 \leq V \leq +1$ were analyzed. The fitting parameters for the *I*/*V* curves were determined to be barrier height (Φ_b) = 1.40–1.49 eV and adjustable parameter (α) = 0.74–0.76. The tunneling decay constant (β) at zero voltage with C12 was estimated to be 0.90–0.94 $Å^{-1}$, which was in good agreement with the previously reported tunneling transport properties of alkanethiol molecules.[31,32]

Fig. 2c shows the *I*/*V* curves for each metal complex using the Pt/Ir tip, which clearly showed different switch voltages according to the central metal atoms. When a positive voltage is applied to a substrate, electron transfer from an STM tip to a molecule on the surface occurs through an empty orbital LUMO, resulting in the trapping or storage of electrons.[5,33] Resonant tunneling through the molecular junction involved in the redox processes can occur by aligning the intrinsic electronic levels of the molecule to the Fermi level of the metal tips.[1,10] The large current hysteresis indicates that the charge could be stored in the molecular reduction states. Furthermore, histograms of threshold conductance voltage from a low-conducting state to a high-conducting state showed distinct conductance states corresponding to the electron affinity levels of metal complexes

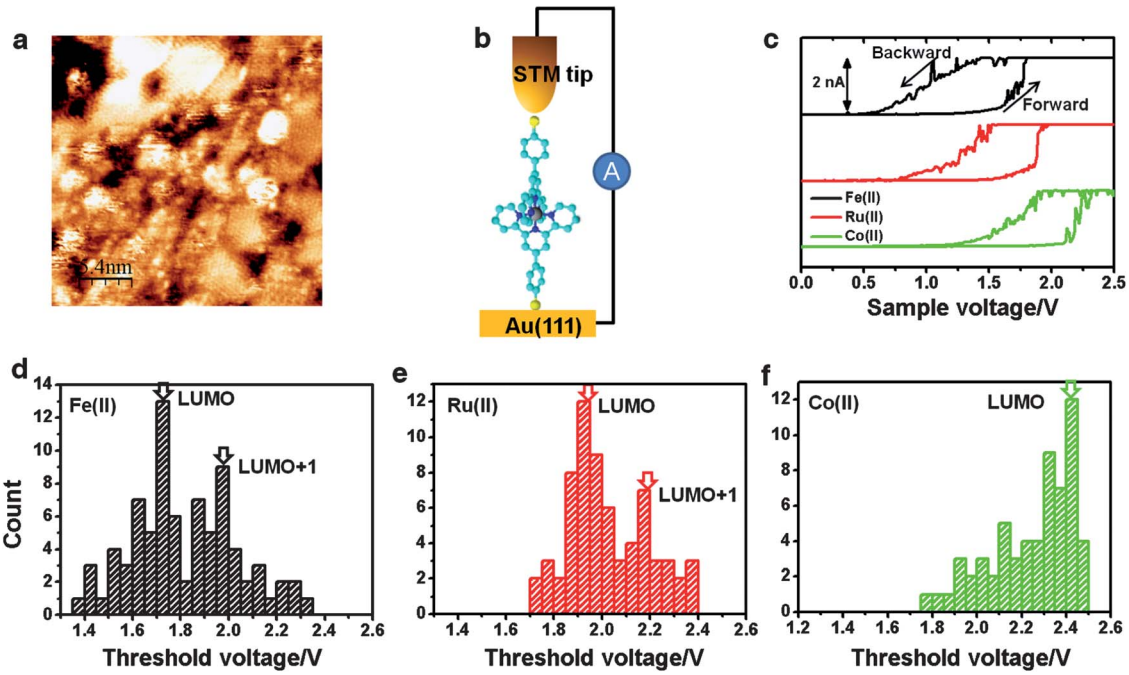

Fig. 2 (a) STM image of a mixed SAM of $Ru^{II}(tpyphs)_2$/1-dodecanethiol (C12) at a constant voltage of 1.5 V_{sample}. *Image condition*: set-point = 15 pA, tip = Pt/Ir. *Image size*: 28 × 28 nm^2. (b) Illustration of a single-molecule junction (*e.g.*, STM tip/molecule/Au). (c) *I*/*V* curves of $M_T^{II}(tpyphs)_2$ at the Pt/Ir tip contact; current responses to voltage sweeping from 0.0 V to V_{sample} in a cycle. (d)–(f) Histograms of the threshold conductance voltage for conductance switching from a low-conducting state to a high-conducting state in *I*/*V* curves of each complex.

(Fig. 2d–f). For example, conductance switching events for the Fe^{II} and Ru^{II} complexes were primarily separated into two distributions corresponding to the energy gaps between the metal contact Fermi level and the electronic energy levels denoted LUMO and LUMO + 1. The histograms for the first switch voltage to LUMO show that Fe^{II}, Ru^{II}, and Co^{II} complexes switched at 1.725 (±0.025) V, 1.925 (±0.025) V, and 2.425 (±0.025) V, respectively, during the 0 V to $+V_{sample}$ sweep. The second statistical distribution for the switch voltage (to LUMO + 1), slightly separated from that of the first one (LUMO), was assigned values of 1.975 (±0.025) V for the Fe^{II} complex and 2.175 (±0.025) V for the Ru^{II} complex. However, the Co^{II} complex showed only one conductance switching type.

Furthermore, using the Au tip, the conductance switching voltage of metal complexes was also measured in STS from the mixed SAMs with C12 (Fig. 3). The protrusions in STM images (Fig. 3a) indicate the metal complexes. The voltage-driven conductance switching of Fe^{II} and Ru^{II} complexes in the Au tip junctions was separated into three distributions in the STS measurements (see Fig. 3b and c and the corresponding *I*/*V* curves in Fig. S2a and b†). The conductance switching events occurred primarily at 1.375 (±0.025) V for the Fe^{II} complex and 1.525 (±0.025) V for the Ru^{II} complex, which corresponded to the energy gaps related to electron transport into LUMO. Those at 1.675 (±0.025) V and 2.075 (±0.025) V (for the Fe^{II} complex) and 1.725 (±0.025) V and 2.125 (±0.025) V (for the Ru^{II} complex) correspond to the energy gaps related to electron transport into LUMO + 1 and LUMO + 2, respectively. For the Co^{II} complex, one conductance switching type was observed, corresponding to the energy gap related to electron transport into LUMO at 2.125 (±0.025) V (see Fig. 3d and the corresponding *I*/*V* curve in Fig. S2c†). The switching voltages for each metal complex in the Au tip junctions were positively shifted by 0.3–0.4 V from those measured at the Pt/Ir tip junction, which may represent the energy gap between the two STM tips. Because of the energy difference between the Fermi levels of the Au and Pt/Ir tips, the detectable conductance states of the metal complexes at the Au tip junctions were higher than those in Pt/Ir tip junctions.

In STM measurement, a metal–molecule–metal junction is simply a diode. Molecular redox states exist when a bias voltage is applied between two metal electrodes. Electron charging onto the molecular redox states corresponds to tunnelling probabilities between the metal electrode and molecules. Therefore, the number of molecules in each high conducting state indicates the population of the corresponding reduced molecules in the molecular monolayers. Furthermore, *I*/*V* characteristics of the charged molecules (at a high conducting state) after conductance switching showed ohmic conduction behavior[17] but not further conductance switching. Thus, conductance switching between the redox states cannot be observed.

Multilevel conductance switching at Au/rGO contacts

In addition to single-molecule measurements using STM, monolayer molecular devices were also fabricated to probe electronic conductance states of the metal complexes in the monolayer-based junctions. Similar to a graphene sheet, an rGO sheet is a thin conductive sheet composed of a single atomic layer of pure sp^2-bonded carbon atoms (Fig. S1†).[34] It is an excellent conducting material that is comparable to a gold electrode for organic electronics applications.[35–37] From *I*/*V* curves of Au/rGO

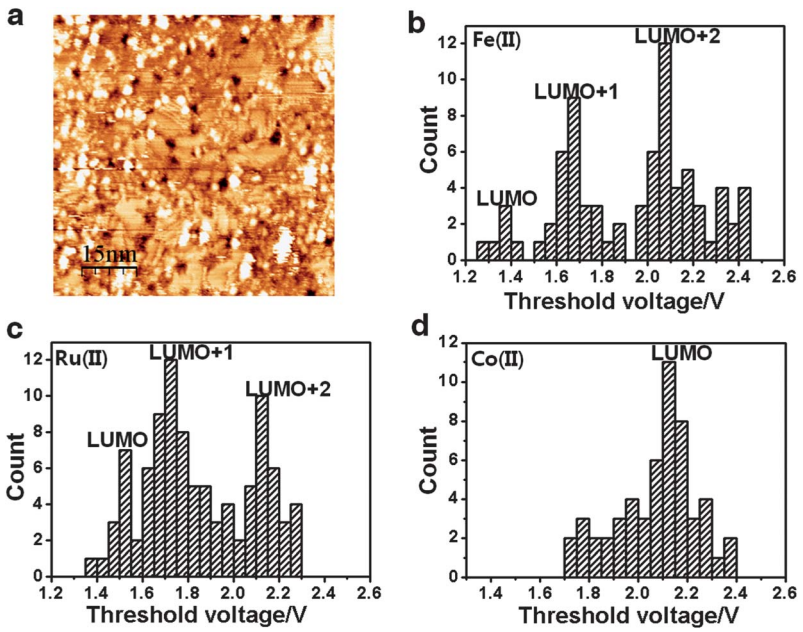

Fig. 3 (a) STM image of a mixed SAM of $Ru^{II}(tpyphs)_2$/1-dodecanethiol (C12) at a constant voltage of 1.5 V_{sample}. *Image conditions*: set-point = 15 pA, tip = Au. *Image size*: 79 × 79 nm^2. (b)–(d) Histograms of the threshold voltage in STS of $M_T^{II}(tpyphs)_2$ at the Au tip contact (see Fig. S2† for corresponding *I*/*V* curves).

film/Au devices, the contact resistance value of the rGO film used in this study was measured to be 160 (±5) Ω at 1.0 V with 95% confidence as measured on 50 devices (Fig. 4a). No current hysteresis or conductance switching was observed in the control samples without molecules. The thickness of the rGO film was measured to be ~20 nm, as shown in Fig. S3†. A conducting interlayer of the rGO thin film can protect the SAMs from hot metal nanoparticles[38,39] during metal vapor deposition forming the top electrode. This allows formation of a stable electronic contact such as carbon nanotubes[40] or graphene films[28] (Fig. 4b).

Fig. 4c shows conductance switching events and current hysteresis observed in monolayer-based devices of the Fe^{II} complex SAM. In terms of threshold conductance voltage, the typical *I*/*V* curves of monolayer-based devices for the Fe^{II} complex can be classified into three types. The primary threshold conductance voltage was obtained by statistical analysis of more than 100 devices (Fig. 4d). At the Au/rGO film contact in the

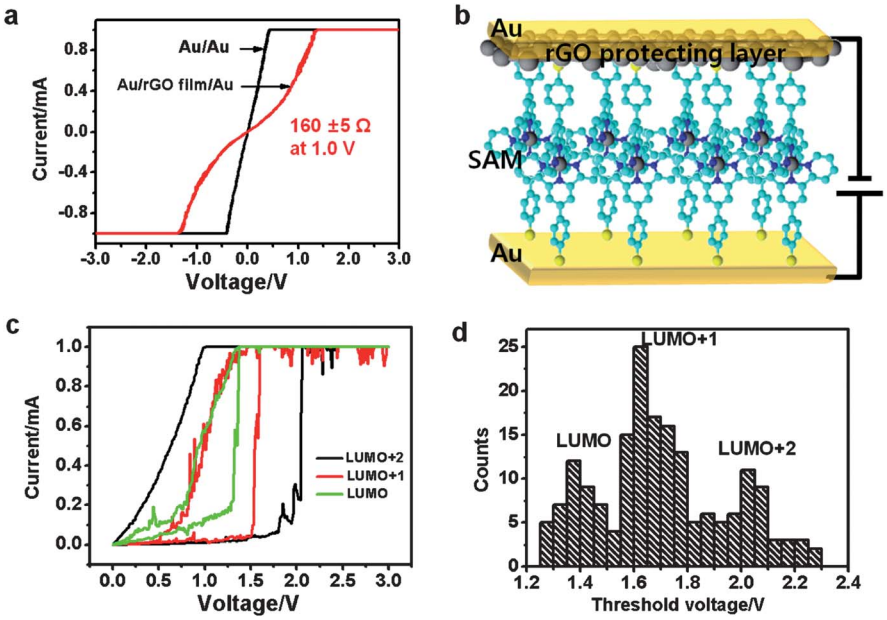

Fig. 4 (a) *I*/*V* characteristics of Au/Au (black curve) and Au/rGO film/Au (red curve) junctions. (b) Illustration of an Au/rGO contact for an Au/rGO film/SAM/Au device. (c) *I*/*V* curves and (d) statistical distributions of the threshold voltage in Au/rGO film/$Fe^{II}(tpyphs)_2$ SAM/Au devices, showing three distinguishable conductance states.

devices of the Fe^{II} complex, 1.375 (±0.025) V, 1.625 (±0.025) V, and 2.025 (±0.025) V were representative threshold conductance voltages. Furthermore, three threshold voltage values of 1.525 (±0.025) V, 1.725 (±0.025) V, and 2.075 (±0.025) V were observed in the devices of the Ru^{II} complex (Fig. S4a and b†), while one threshold voltage value of 2.10 (±0.05) V was observed in the devices of the Co^{II} complex (Fig. S4c and d†). Threshold conductance voltages through the Au/rGO film contact of the M_T^{II} complex SAMs are identical with those through the Au tip contact of STM-based molecular junctions, indicating that an Au/rGO film electrode is comparable to an Au electrode, consistent with the results of a previous report.[41]

Central metal-dependent multiple electroreduction of metal complexes

The molecular orbital energies corresponding to the ionization energy levels and the electron affinity levels of redox-active molecules can be estimated by solution-phase electrochemistry.[42,43] The redox behaviors of M_T^{II}(bisterpyridine) (*e.g.*, $M_T^{II}(tpy)_2$) derivatives were dominated by M^{2+}/M^{3+} and tpy/tpy^-/tpy^{2-}/tpy^{3-} redox couples, as shown in Fig. 5.[44] During voltage sweeping in the negative potential direction, there are reversible redox couples and irreversible reduction/adsorption peaks. Three redox peaks ($M^{II}tpy/M^{II}tpy^-/M^{II}tpy^{2-}/M^{II}tpy^{3-}$) for the ligand overlapped slightly with the $M^{2+}/M^+/M^0$ redox couples and adsorption peaks. Therefore, each peak potential was assigned using several cyclic voltammograms (CVs) obtained with different voltage sweep directions. If the reduced metal complexes are adsorbed (or deposited) on the electrode surface, the reaction peaks are irreversible (*e.g.*, M^{2+}/M^+ or M^+/M^0). We determined the reaction continuity/relation between each redox peak in this study. As a result, the peaks of M^{2+}/M^{3+} and M^{2+}/M^+ are correlated with each other, as are the peaks of tpy/tpy^-, tpy^-/tpy^{2-}, and tpy^{2-}/tpy^{3-} in the CVs. The electrochemical oxidation potentials corresponded to the ionization energy of the metal complex of the metal-centered HOMO.[7,45–47] Also, the electrochemical reduction potentials corresponded to the electron affinity energy of the metal complex, which belonged to the ligand-centered LUMO.[7,45–47] The energies of the ground-state HOMO were calculated using the redox potentials of the Fe^{2+}/Fe^{3+} redox couples ($E_{1/2}$ = 1.15 (±0.02) V_{SCE} *versus* saturated calomel electrode (SCE)), Ru^{2+}/Ru^{3+} redox couples ($E_{1/2}$ = 1.32 (±0.02) V_{SCE}), and Co^{2+}/Co^{3+} redox couples ($E_{1/2}$ = 0.35 (±0.02) V_{SCE}). The energies of the ground-state LUMOs were estimated using the potentials of tpy/tpy^-/tpy^{2-}/tpy^{3-} redox couples, which were varied according to the central metal atoms. The potentials were assigned as tpy/tpy^- ($E_{1/2}$ = −0.90 (±0.02) V_{SCE}), tpy^-/tpy^{2-} ($E_{1/2}$ = −1.20 (±0.02) V_{SCE}), and tpy^{2-}/tpy^{3-} ($E_{1/2}$ = −1.46 (±0.02) V_{SCE}) for the Fe^{II} complex and tpy/tpy^- ($E_{1/2}$ = −0.98(±0.02) V_{SCE}), tpy^-/tpy^{2-} ($E_{1/2}$ = −1.15 (±0.02) V_{SCE}), and tpy^{2-}/tpy^{3-} ($E_{1/2}$ = −1.38 (±0.02) V_{SCE}) for the Ru^{II} complex, while only one redox couple, tpy/tpy^- ($E_{1/2}$ = 1.82 (±0.02) V_{SCE}) was observed for the Co^{II} complex in the electrochemical potential window. Table 1 shows the metal-centered HOMO energies and the ligand-centered LUMO energies at the vacuum level, which were calculated by energy conversion of solution-phase electrochemical potentials. The vacuum level corresponding to the molecular orbitals can be calculated according to

$$V_{abs}\ (eV) = 4.7\ eV + E_{1/2},$$

where $E_{1/2}$ is the redox formal potential *versus* SCE, and 4.7 eV is approximated according to the vacuum level for SCE.[47]

In addition, the LUMO can have either a metal (σ^*_M) or ligand (π^*_L) center, depending on the relative energy order. From UV-Vis spectroscopy, as shown in Fig. 1b, for each complex which shows an absorption peak of the metal-to-ligand charge transfer (π_M to π^*_L), we can assume the energy gap between LUMO (π^*_L) and HOMO (π_M) levels in the configuration of molecular orbitals. As a result, the energy gap of LUMO–HOMO in UV-Vis spectroscopy is in agreement with the energy gap between the peak of tpy/tpy^- and the peak of M^{2+}/M^{3+} in CVs (Table 1). Consequently, the LUMO should be the ligand-centered π^*_L orbital.

The estimated energy gaps between the metal contact Fermi level and LUMO energy levels at each contact are shown in Table 2. Consequently, the molecular charged energy at the electron affinity levels of the redox-active metal complexes calculated from the results of CVs were in good agreement with those measured by STM and the monolayer-based junctions.

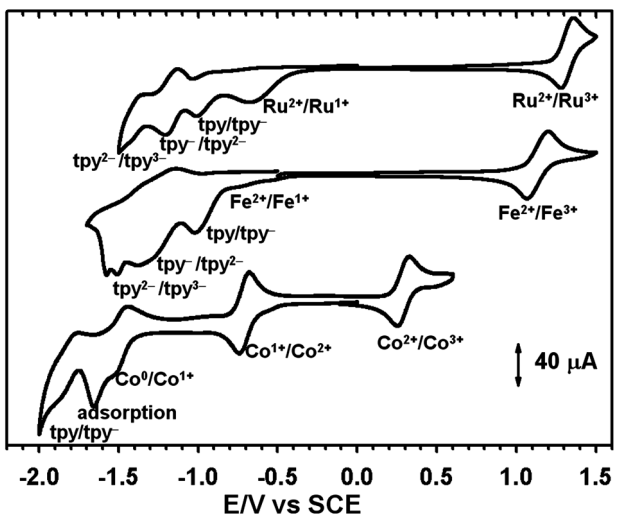

Fig. 5 Cyclic voltammograms (CVs) of 3.0 mM $M_T^{II}(tpyphs)_2$ complexes; M^{2+}/M^{3+} and tpy/tpy^-/tpy^{2-}/tpy^{3-} redox couples were assigned in 0.1 M $TBAPF_6$/acetonitrile at 0.1 V s^{-1}.

Table 1 Molecular energy levels of $M_T^{II}(tpyphs)_2$ measured in CVs (Fig. 5) with respect to the vacuum level. The error range is ±0.02 eV

Redox couples/molecular orbital	Co^{II} Energy levels/eV	Fe^{II}	Ru^{II}
M^{2+}/M^{3+}/HOMO	−5.05	−5.85	−6.02
tpy/tpy^-/LUMO	−2.88	−3.80	−3.72
tpy^-/tpy^{2-}/LUMO + 1		−3.50	−3.55
tpy^{2-}/tpy^{3-}/LUMO + 2		−3.25	−3.30
Molecular orbital/measurement	**Co^{II} Energy gap/eV**	**Fe^{II}**	**Ru^{II}**
HOMO–LUMO/CV	2.17	2.05	2.30
HOMO–LUMO/UV	2.19	2.02	2.32

Table 2 Energy gaps (eV) between the metal Fermi levels (Pt/Ir = ~5.6 eV[48] and Au = ~5.1 eV[7]) and the electron affinity levels (LUMO levels) obtained in CVs were compared with the threshold voltages measured by *I*/*V* (given in parentheses)

	Co^{II}			Fe^{II}			Ru^{II}		
	Metal contact								
	Threshold conductance voltage (eV) estimated from CV[a] and *I*/*V*[b]								
Electron affinity level (or molecular orbital)	Pt/Ir	Au	Au/rGO	Pt/Ir	Au	Au/rGO	Pt/Ir	Au	Au/rGO
LUMO	2.72 (2.425)	2.22 (2.125)	(2.10)	1.80 (1.725)	1.30 (1.375)	(1.375)	1.88 (1.925)	1.38 (1.525)	(1.525)
LUMO + 1				2.10 (1.975)	1.64 (1.675)	(1.625)	2.05 (2.175)	1.55 (1.725)	(1.725)
LUMO + 2				2.35	1.85 (2.075)	(2.025)	2.30	1.70 (2.125)	(2.075)

[a] The error range is ±0.02 eV. [b] The error range is ±0.025 eV.

Thus, the electron affinity energy levels of the M_T^{II} complexes measured in the solid-state junctions were comparable to their LUMO energy levels measured in solution. The first and second electron affinity energies for the Fe^{II} and Ru^{II} complexes at the Pt/Ir contacts were consistent with the molecular reduction states obtained by CVs. However, the molecular charged energy to the LUMO of the Co^{II} complex showed a downward shift in both Pt/Ir and Au tip contacts. If an image charge is induced by the Co^{II} complex on a metal surface whose HOMO level can be coupled to the metal surface, it leads to a relatively high conductivity.[20] Thus, electron trapping LUMO levels will approach the HOMO levels, which can result in a shift in the molecular orbital levels and a reduction in the effective gap.[9] The downward shift of ~0.3 eV in the Co^{II} complex indicates strong coupling with metal contacts, which is consistent with a previous report.[11] Furthermore, the molecular charged energies to LUMO + 1 and LUMO + 2 for the Ru^{II} complex and to LUMO + 2 for the Fe^{II} complex were measured by the upward shift in the Au tip and Au/rGO film contacts, which may be due to weak coupling effects between the metal contacts and molecules in the molecular junctions.

Conclusions

In summary, redox-active transition metal (*e.g.*, Fe^{II}, Ru^{II}, and Co^{II}) complexes having terpyridine ligands with a conjugated phenyl linker can drive energy state localization of LUMOs. *I*/*V* characteristics taken at the molecular junctions of the Fe^{II} and Ru^{II} complexes showed three conductance switching events, which represent three discriminative LUMO levels that access electrons from the metal contacts in the STM- and the Au/rGO film/monolayer-based junctions. The multiple electron affinity levels of the metal complex molecules have been confined to intrinsic molecular levels, consistent with the observed molecular reduction states of the molecules obtained by electrochemistry. Thus, electron transport properties of redox-active molecules with multiple reduction states suggest multilevel molecular memory components. The reliable and stable junctions, using a soft electrode with an rGO film as a part of the top electrode, can be used for investigation of molecular electronics without forming a metal filament short circuit.

Acknowledgements

This work was supported by the Creative Research Initiatives (project title: Smart Molecular Memory) of MEST/NRF.

Notes and references

1 J. He, Q. Fu, S. Lindsay, J. W. Ciszek and J. M. Tour, *J. Am. Chem. Soc.*, 2006, **128**, 14828–14835.
2 R. L. McCreery, *Chem. Mater.*, 2004, **16**, 4477–4496.
3 S. Kubatkin, A. Danilov, M. Hjort, J. Cornil, J.-L. Bredas, N. Stuhr-Hansen, P. Hedegard and T. Bjornholm, *Nature*, 2003, **425**, 698–701.
4 K. Liu, X. Wang and F. Wang, *ACS Nano*, 2008, **2**, 2315–2323.
5 Z. Ng, K. P. Loh, L. Li, P. Ho, P. Bai and J. H. K. Yip, *ACS Nano*, 2009, **3**, 2103–2114.
6 A. S. Blum, T. Ren, D. A. Parish, S. A. Trammell, M. H. Moore, J. G. Kushmerick, G. L. Xu, J. R. Deschamps, S. K. Pollack and R. Shashidhar, *J. Am. Chem. Soc.*, 2005, **127**, 10010–10011.
7 K. Seo, A. V. Konchenko, J. Lee, G. S. Bang and H. Lee, *J. Am. Chem. Soc.*, 2008, **130**, 2553–2559.
8 C. Li, W. Fan, D. A. Straus, B. Lei, S. Asano, D. Zhang, J. Han, M. Meyyappan and C. Zhou, *J. Am. Chem. Soc.*, 2004, **126**, 7750–7751.
9 A. K. Mahapatro, J. Ying, T. Ren and D. B. Janes, *Nano Lett.*, 2008, **8**, 2131–2136.
10 R. A. Wassel, G. M. Credo, R. R. Fuierer, D. L. Feldheim and C. B. Gorman, *J. Am. Chem. Soc.*, 2004, **126**, 295–300.
11 J. Park, A. N. Pasupathy, J. I. Goldsmith, C. Chang, Y. Yaish, J. R. Petta, M. Rinkoski, J. P. Sethna, H. D. Abruna, P. L. McEuen and D. C. Ralph, *Nature*, 2002, **417**, 722–725.
12 S. Tsoi, I. Griva, S. A. Trammell, A. S. Blum, J. M. Schnur and N. Lebedev, *ACS Nano*, 2008, **2**, 1289–1295.
13 W. Haiss, H. van Zalinge, S. J. Higgins, D. Bethell, H. HÄbenreich, D. J. Schiffrin and R. J. Nichols, *J. Am. Chem. Soc.*, 2003, **125**, 15294–15295.
14 F. Chen, J. He, C. Nuckolls, T. Roberts, J. E. Klare and S. Lindsay, *Nano Lett.*, 2005, **5**, 503–506.
15 X. Xiao, L. A. Nagahara, A. M. Rawlett and N. Tao, *J. Am. Chem. Soc.*, 2005, **127**, 9235–9240.
16 T. Albrecht, A. Guckian, A. M. Kuznetsov, J. G. Vos and J. Ulstrup, *J. Am. Chem. Soc.*, 2006, **128**, 17132–17138.
17 K. Seo, A. V. Konchenko, J. Lee, G. S. Bang and H. Lee, *J. Mater. Chem.*, 2009, **19**, 7617–7624.
18 B. Pradhan and S. Das, *Chem. Mater.*, 2008, **20**, 1209–1211.
19 C. Li, J. Ly, B. Lei, W. Fan, D. Zhang, J. Han, M. Meyyappan, M. Thompson and C. Zhou, *J. Phys. Chem. B*, 2004, **108**, 9646–9649.
20 N. Tuccitto, V. Ferri, M. Cavazzini, S. Quici, G. Zhavnerko, A. Licciardello and M. A. Rampi, *Nat. Mater.*, 2009, **8**, 41–46.
21 N. Joo, S. Renaudineau, G. Delapierre, G. Bidan, L. M. Chamoreau, R. Thouvenot, P. Gouzerh and A. Proust, *Chem.–Eur. J.*, 2010, **16**, 5043–5051.
22 A. Bandyopadhyay and K. Miki, *Adv. Funct. Mater.*, 2008, **18**, 1173–1177.
23 Z. Liu, A. A. Yasseri, J. S. Lindsey and D. F. Bocian, *Science*, 2003, **302**, 1543–1545.
24 V. C. Tung, M. J. Allen, Y. Yang and R. B. Kaner, *Nat. Nanotechnol.*, 2009, **4**, 25–29.
25 X. Wang, L. Zhi and K. Müllen, *Nano Lett.*, 2008, **8**, 323–327.
26 D. Li, M. B. Müller, S. Gilje, R. B. Kaner and G. G. Wallace, *Nat. Nanotechnol.*, 2008, **3**, 101–105.

27 G. Eda and M. Chhowalla, *Adv. Mater.*, 2010, **22**, 2392–2415.
28 G. Wang, Y. Kim, M. Choe, T. W. Kim and T. Lee, *Adv. Mater.*, 2011, **23**, 755–760.
29 J. G. Simmons, *J. Appl. Phys.*, 1963, **34**, 1793–1803.
30 W. Wang, T. Lee and M. A. Reed, *Phys. Rev. B: Condens. Matter Mater. Phys.*, 2003, **68**, 354161–354167.
31 L. A. Bumm, J. J. Arnold, T. D. Dunbar, D. L. Allara and P. S. Weiss, *J. Phys. Chem. B*, 1999, **103**, 8122–8127.
32 D. J. Wold and C. D. Frisbie, *J. Am. Chem. Soc.*, 2001, **123**, 5549–5556.
33 S. Datta, W. Tian, S. Hong, R. Reifenberger, J. I. Henderson and C. P. Kubiak, *Phys. Rev. Lett.*, 1997, **79**, 2530–2533.
34 G. Eda, G. Fanchini and M. Chhowalla, *Nat. Nanotechnol.*, 2008, **3**, 270–274.
35 K. S. Novoselov, A. K. Geim, S. V. Morozov, D. Jiang, M. I. Katsnelson, I. V. Grigorieva, S. V. Dubonos and A. A. Firsov, *Nature*, 2005, **438**, 197–200.
36 Y. Zhang, Y. W. Tan, H. L. Stormer and P. Kim, *Nature*, 2005, **438**, 201–204.
37 A. K. Geim and K. S. Novoselov, *Nat. Mater.*, 2007, **6**, 183–191.
38 A. V. Walker, T. B. Tighe, O. M. Cabarcos, M. D. Reinard, B. C. Haynie, S. Uppili, N. Winograd and D. L. Allara, *J. Am. Chem. Soc.*, 2004, **126**, 3954–3963.
39 G. L. Fisher, A. V. Walker, A. E. Hooper, T. B. Tighe, K. B. Bahnck, H. T. Skriba, M. D. Reinard, B. C. Haynie, R. L. Opila, N. Winograd and D. L. Allara, *J. Am. Chem. Soc.*, 2002, **124**, 5528–5541.
40 J. He, B. Chen, A. K. Flatt, J. J. Stephenson, C. D. Doyle and J. M. Tour, *Nat. Mater.*, 2006, **5**, 63–68.
41 S. Pang, H. N. Tsao, X. Feng and K. Mullen, *Adv. Mater.*, 2009, **21**, 3488–3491.
42 E. W. Wong, C. P. Collier, M. Běhloradský, F. M. Raymo, J. F. Stoddart and J. R. Heath, *J. Am. Chem. Soc.*, 2000, **122**, 5831–5840.
43 W. Han, E. N. Durantini, T. A. Moore, A. L. Moore, D. Gust, P. Rez, G. Leatherman, G. R. Seely, N. Tao and S. M. Lindsay, *J. Phys. Chem. B*, 1997, **101**, 10719–10725.
44 R. D. Rakhimov, Y. A. Weinstein, E. V. Lileeva, N. N. Zheligovskaya, M. Y. Mel'nikov and K. P. Butin, *Russ. Chem. Bull.*, 2003, **52**, 1150–1156.
45 M. R. Adam, J. H. Theresa, A. N. Larry, K. T. Raymond, K. R. Ganesh and M. L. Stuart, *Appl. Phys. Lett.*, 2002, **81**, 3043–3045.
46 V. Balzani, A. Juris, M. Venturi, S. Campagna and S. Serroni, *Chem. Rev.*, 1996, **96**, 759–834.
47 K. W. Hipps, in *Handbook of Applied Solid State Spectroscopy*, ed. D. R. Vij, Springer Verlag, New York, 2006, vol. 7, pp. 305–350.
48 K. Kitagawa, T. Morita and S. Kimura, *Langmuir*, 2005, **21**, 10624–10631.